RESEARCH ARTICLE

Complexant-facilitated assembly of NiTiO₃ nanoparticles into microbars for high-performance lithium-ion battery anode

Meng Sun[1] | Xiaoli Sheng[1] | Zhipeng Cui[1] | Sijie Li[1] | Qingye Zhang[1] |
Fei Xie[1] | Guanting Liu[1] | Shujin Hao[1] | Feiyu Diao[2] | Shiduo Sun[3] |
Yiqian Wang[1]

[1]College of Physics, Qingdao University, Qingdao, People's Republic of China

[2]Industrial Research Institute of Nonwovens and Technical Textiles, Shandong Engineering Research Center for Specialty Nonwoven Materials, College of Textiles and Clothing, Qingdao University, Qingdao, People's Republic of China

[3]State Key Laboratory, Qingdao University, Qingdao, People's Republic of China

Correspondence
Yiqian Wang, College of Physics, Qingdao University, Qingdao 266071, People's Republic of China.
Email: yqwang@qdu.edu.cn

Feiyu Diao, Industrial Research Institute of Nonwovens and Technical Textiles, Shandong Engineering Research Center for Specialty Nonwoven Materials, College of Textiles and Clothing, Qingdao University, Qingdao 266017, People's Republic of China.
Email: fydiao@qdu.edu.cn

Funding information
National Natural Science Foundation of China, Grant/Award Number: 10974105; Shandong Province "Double-Hundred Talent Plan" Program, Grant/Award Number: WST2018006; High-end foreign experts project of the Ministry of Science and Technology, China, Grant/Award Numbers: G2022025015L, G2022025016L

Abstract

Nickel titanate (NiTiO₃) nanostructured materials have gained extensive attention in the field of lithium-ion batteries (LIBs) due to their high theoretical capacity and low cost. However, NiTiO₃ exhibits low conductivity and significant volume changes during cycling, resulting in capacity decay and poor cycling stability. Herein, we propose a feasible strategy to enhance the cycling performance of NiTiO₃ nanostructures by adjusting their morphology. By manipulating the choice of solvent employed in the synthetic process, we obtain NiTiO₃ microbars (NTO MBs) through self-assembly of NiTiO₃ nanoparticles (NTO NPs). When utilized as an anode material in LIBs, NTO MBs exhibit a capacity of 410 mAh g^{-1} after 200 cycles at 100 mA g^{-1}, surpassing that of NTO NPs (212 mAh g^{-1}). The improved performance of NTO MBs is attributed to their unique porous bar-like structure, composed of numerous NPs, which provides a substantial storage space for Li^+ ions owing to its larger specific surface area. Additionally, the porous structure accelerates the diffusion of Li^+ ions and electron transfer. To gain a profound understanding of the enhanced performance through morphology adjustment, we conduct a comprehensive investigation on the growth mechanism of NTO MBs. This work provides valuable insights into the mechanism governing the morphology control of NTO MBs, facilitating the rational design and synthesis of tailored materials with enhanced performance for LIBs.

KEYWORDS
electrochemical performance, growth mechanism, lithium-ion battery, microstructure, morphology control, NiTiO₃

1 | INTRODUCTION

The energy storage technology for renewable resources is of growing significance in the scientific community. Lithium-ion batteries (LIBs) are highly regarded as advanced energy storage devices and have extensive applications in portable power electronics, electric vehicles, and smart grids.[1–8] Transition metal oxides (TMO), known for their large theoretical capacity, high energy density, and cost-effectiveness, are considered as promising electrode materials.[9–14] Among them, titanium-based oxides have garnered considerable attention due to small volume change during the lithium-ion insertion/extraction process, resulting in exceptional structural stability and prolonged battery endurance.[15–17] As a typical representative of titanium-based anodes, TiO_2 exhibits excellent cycling stability with a volume change of less than 4% during cycling.[18–20] However, TiO_2 possesses a theoretical capacity of 335 mAh g^{-1}, lower than that of commercial graphite (372 mAh g^{-1}), which hinders its further development.[21,22]

Recently, perovskite-structured transition metal titanates ($MTiO_3$, M = Fe, Co, Ni) have attracted widespread attention due to the joint participation of TMOs and titanium dioxide in redox reactions, resulting in high theoretical capacity.[23–25] Within this category, nickel titanate ($NiTiO_3$) demonstrates a high theoretical capacity of 500 mAh g^{-1} and has been reported as a promising anode material for LIBs.[25,26] However, the $NiTiO_3$ electrode encounters challenges such as low electrical conductivity and significant volume expansion brought by nickel oxides during cycling, resulting in capacity degradation and poor cycling stability.[25,26] To address these limitations, composite materials are commonly employed to enhance the electrochemical performance of $NiTiO_3$, particularly its electrical conductivity, such as $NiTiO_3$/reduced graphene oxide nanocomposite[27] and $NiTiO_3$/TiO_2 nanocomposite.[16] Nevertheless, this approach often compromises the lithium storage capacity of the material and frequently necessitates complex synthesis process. Alternatively, an advantageous strategy for improving the electrochemical performance of TMOs is to increase lithium storage sites through designing different morphologies and microstructures. For instance, Huang et al.[28] enhanced the rate capability and cycling performance of both sodium and LIBs by preparing mesoporous $NiTiO_3$ micro-prisms. Zou et al.[29] bolstered the conductivity and stability of electrodes for Li-storage by synthesizing mesoporous $ZnMn_2O_4$ nano-peanuts. Tang et al.[30] improved specific capacity and cycling stability through designing porous $CoTiO_3$ microbars (MB). Notably, the bar-like and porous structure offers advantages due to its large specific surface area, short Li$^+$ diffusion path, and excellent cyclic stability.[30] Despite these advancements, there are currently few relevant studies on the electrochemical performance enhancement of bar-shaped $NiTiO_3$.

In this work, $NiTiO_3$ microbars (NTO MBs) were prepared through self-assembly of $NiTiO_3$ nanoparticles (NTO NPs) during the solvothermal synthesis process. When used as an anode material in LIBs, NTO MBs exhibit better electrochemical performance compared to NTO NPs. The enhanced performance of NTO MBs can be attributed to their unique porous rod-like structure, which is composed of many NPs and provides sufficient storage space for Li$^+$ ions due to large specific surface area of MBs. Moreover, the small NTO NPs within the porous structure serve as bridges for Li$^+$/e^- kinetic diffusion, greatly enhancing both Li$^+$-ion diffusion rate and electron transfer rate. This synergistic effect between the porous structure and the NPs constituents contributes to the improved electrochemical performance of NTO MBs. Furthermore, to gain a deeper understanding of the performance enhancement achieved through morphology adjustment, the growth mechanism of NTO MBs was elucidated.

2 | EXPERIMENTAL

2.1 | Materials' synthesis

NTO MBs and NTO NPs were synthesized by a solvothermal method. In this process, 0.373 g of nickel acetate [NA, $Ni(CH_3COO)_2$] was dissolved into 60 mL ethylene glycol [EG, $(CH_2OH)_2$] and stirred until completely dissolved. Then 510 mL tetrabutyl titanate [TBT, $Ti(OC_4H_9)_4$] was introduced into the solution and stirred at a temperature of 28°C, resulting in the formation of a green-hued solution. After 3 h of stirring, the solution was transferred into a 100 mL autoclave at 160°C and kept for 12 h. The sediments were obtained by centrifugation, washed with ethanol, and dried at 70°C overnight to get green powder, named as the precursor. Subsequently, the precursor was calcinated in tube furnace at 650°C for 2 h in air to obtain the final NTO MBs. This thermal treatment facilitated the transformation of the precursor into yellow powder. For comparison, NTO NPs were prepared following the same process, with the only variation being the use of absolute ethanol as the solvent instead of EG.

2.2 | Materials' characterization

The morphologies were examined by a field-emission scanning electron microscope (FESEM). Crystal structures were characterized with SmartLab X-ray

diffraction (XRD) with Cu Kα_1 radiation ($\lambda = 0.15406$ nm). Raman spectra were collected by a microscopic confocal spectrometer (Renishaw PLC). Bright field (BF), high-resolution transmission electron microscope (HRTEM) images, and selected area electron diffraction (SAED) patterns were performed on JEOL JEM2100F TEM. Adsorption and desorption isotherms of nitrogen were measured by NOVA 1100 volumetric sorption analyzer. The specific surface area and pore size distributions were analyzed by Brunauer–Emmett–Teller and Barrett–Joyner–Halenda methods, respectively.

2.3 | Electrochemical measurements

NTO MBs (or NTO NPs) were used as active materials to prepare the anodes of CR2025-type button batteries. They were mixed with carbon black and polyvinylidene fluoride (PVDF) in a mass ratio of 7:2:1 on copper foil. CR2025 button batteries were assembled in a high-purity argon glove box with moisture and oxygen concentrations of less than 0.1 ppm. Lithium foil was used as a counter electrode. N-methylpyrrolidone (NMP) served as solvent. The electrolyte consists of 1 M LiPF$_6$ solution of ethylene carbonate (EC)/dimethyl carbonate (DMC)/diethyl carbonate (DEC) (1:1:1 in volume). The electrochemical performances were measured using a LAND CT2001 battery test system in the voltage range of 0.01–3.00 V. Cyclic voltammetry (CV) measurements within the potential range of 0.01–3.00 V at a scan rate of 0.3 mV s^{-1} and electrochemical impedance spectroscopy (EIS) tests at 100 kHz to 0.01 Hz frequency range with a disturbance amplitude of 10 mV were performed on a Metrohm Autolab electrochemical workstation (PGSTAT 302).

3 | RESULTS AND DISCUSSION

Figure 1A,C shows typical SEM images of NTO NPs at different magnifications. The average diameter of NTO NPs is about 75 nm with uniform size. Figure 1B,D exhibits SEM images of NTO MBs, which display a distinctive bar-shaped morphology. The average length and diameter of the NTO MBs are approximately 1.25 μm and 180 nm, respectively. Figure 1D reveals that the NTO MBs consist of numerous NPs, some of which are highlighted with red lines. Figure 1E,F presents size distributions for NTO NPs and MBs, respectively. The NTO NPs exhibit a size distribution ranging from 40 to 110 nm, with an average diameter of 75 nm. Conversely, the size distribution of the NPs in NTO MBs ranges from 35 to 75 nm, with an average diameter of 55 nm. Consequently, it can be inferred that the diameter

of NPs in NTO MBs is smaller than that of the synthetic NTO NPs.

Figure 2 presents typical XRD patterns and Raman spectra of NTO NPs and MBs. Figure 2A illustrates that all observed diffraction peaks align precisely with the rhombohedral NTO (JCPDS no.: 33-0960).[26] The absence of any additional impurity peaks indicates the high purity of the synthesized products. The sharp and well-defined diffraction peaks in all XRD patterns imply excellent crystallinity for both NTO MBs and NPs. The Raman spectra depicted in Figure 2B demonstrate that 11 Raman peaks of both NTO NPs and MBs are consistent with those reported in the previous literature.[31,32] The prominent Raman peak observed at 705 cm^{-1} corresponds to the strongest vibrational mode of NiO$_6$ octahedra.[31–33] No additional peaks are identified in Raman spectra, further confirming the pure NTO composition of synthesized samples.

The microstructure of NTO NPs and MBs was extensively examined using TEM and HRTEM. Figure 3A shows that the NTO NPs have a highly uniform diameter. The SAED pattern in Figure 3B shows a polycrystalline nature, which can be indexed using a rhombohedral NTO ($a = 5.030$ Å, $c = 13.791$ Å). Figure 3C displays a typical HRTEM image of an individual NTO NP, revealing its spherical shape with a diameter of 40 nm. In Figure 3D, the lattice spacings measured from the magnified HRTEM image are 3.68 and 2.70 Å, corresponding to the (0 1 2) and (1 0 4) interplanar spacings of NTO, respectively.

The TEM image of NTO MBs shown in Figure 4A reveals their micron bar-like morphology. The SAED pattern is consistent with the rhombohedral crystal structure of NTO, corroborating the XRD results. The concentric rings observed in the SAED pattern can be indexed to the (0 1 2), (1 0 4), (1 1 0), and (1 1 3) planes of NTO, indicating that the NTO MBs are polycrystalline. Figure 4B presents a TEM image of an individual NTO MB. The measured length and diameter of the rod are about 1.30 μm and 180 nm, respectively. It can be observed from the image that the NTO MBs are composed of smaller NPs. Upon closer examination, numerous pores are found on the surface of the NTO MBs. This porous rod-like structure provides abundant channels for full penetration of electrolyte in NTO MBs electrode, facilitating the rapid transfer of Li$^+$ ions and electrons. The lattice spacings measured in Figure 4D are 2.70, 2.52, and 2.70 Å, which correspond to the (1 0 4), (1 1 0), and (0 $\bar{1}$ 4) planes of NTO, respectively.

The specific surface area and pore size of NTO NPs and MBs were determined through nitrogen adsorption/desorption tests. Figure 5A demonstrates the hysteresis loop of type-IV adsorption/desorption isotherms, indicating the mesoporous nature of both NTO NPs and MBs.[34] In Figure 5B, the predominant pore sizes of NTO NPs and MBs are 10 and 40 nm, respectively. The total pore
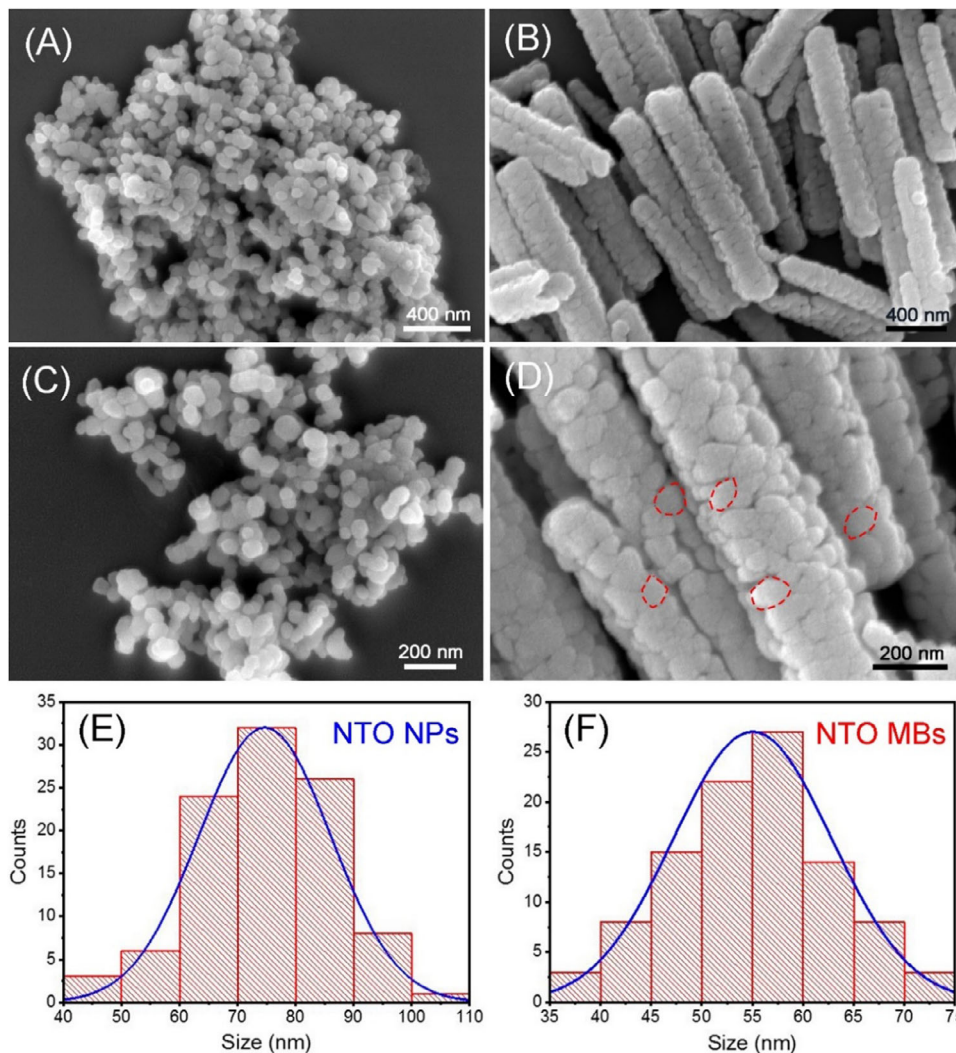
FIGURE 1 SEM images of NTO NPs (A,C) and NTO MBs (B,D). Size distributions of NTO NPs (E) and NPs in NTO MBs (F). MB, microbar; NP, nanoparticle; SEM, Scanning electron microscope.
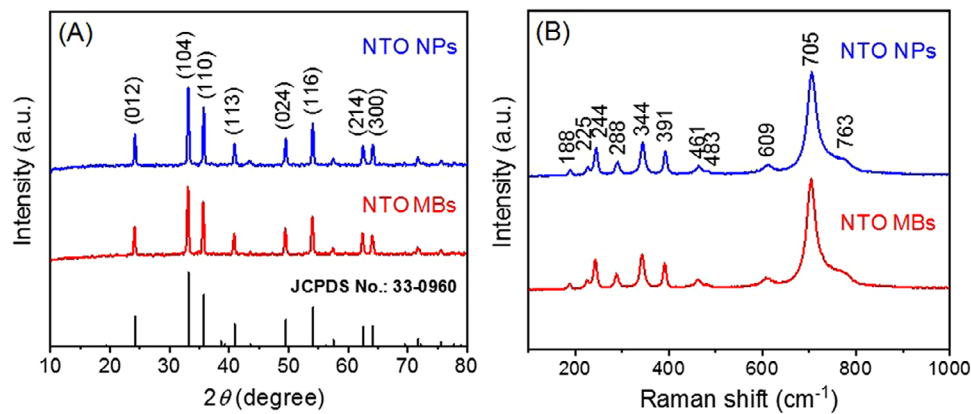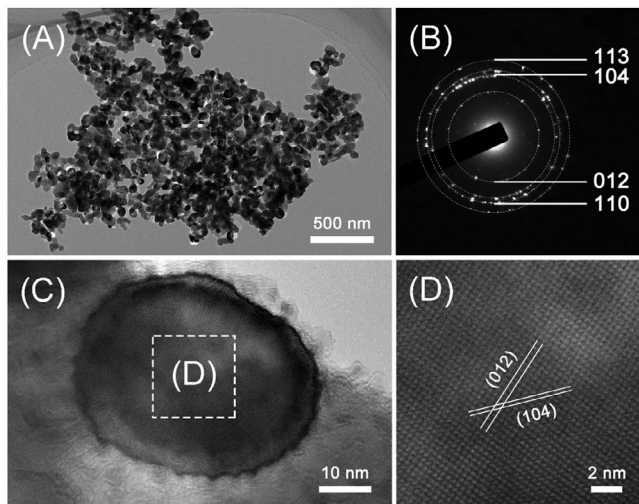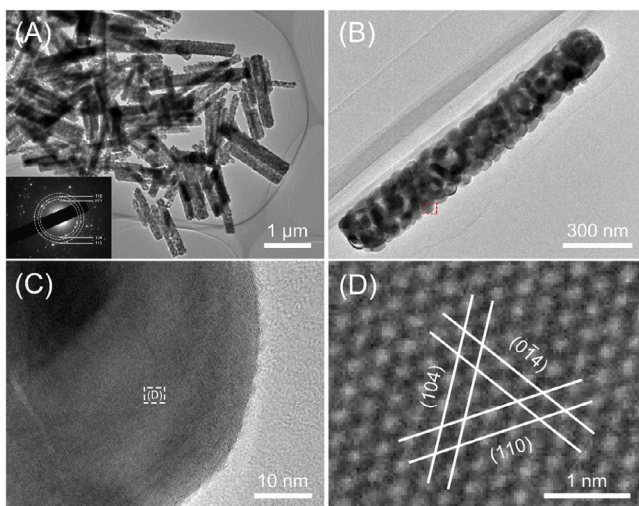

FIGURE 2 XRD patterns (A) and Raman spectra (B) of NTO NPs and MBs. MB, microbar; NP, nanoparticle; XRD, X-ray diffraction.

FIGURE 3 Typical BF image (A) and SAED pattern (B) of NTO NPs. (C) HRTEM image of NTO NP. (D) Enlarged HRTEM image in (C). BF, Bright field; HRTEM, high-resolution transmission electron microscope; NP, nanoparticle; SAED, selected area electron diffraction.

FIGURE 4 (A) BF image of NTO NPs. Inset shows the SAED pattern. (B) TEM image of an individual NTO MB. (C) The image of the area surrounded by a red rectangle in (B). (D) The image of the area surrounded by a white rectangle in (C). BF, Bright field; MB, microbar; SAED, selected area electron diffraction; TEM, transmission electron microscope.

volume of NTO MBs ($0.073 \text{ cm}^3 \text{ g}^{-1}$) surpasses that of NTO NPs ($0.013 \text{ cm}^3 \text{ g}^{-1}$). Furthermore, the specific surface area of NTO MBs is calculated to be $15.11 \text{ m}^2 \text{ g}^{-1}$, which is higher than that of NTO NPs ($7.49 \text{ m}^2 \text{ g}^{-1}$). The larger specific surface area of NTO MBs can provide more reaction sites for Li^+, thereby enhancing lithium storage capacity.

CV tests were conducted to study the electrochemical reaction process. Figure 6A,B exhibits CV curves of NTO electrodes for the first six cycles, respectively. The reduction curve of the first cycle differs from the subsequent five cycles due to a structural change occurring within the anode material, resulting from the formation of a solid electrolyte interface (SEI) film.[35] For the first cycle, CV curves of NTO electrodes exhibit two cathodic peaks. The peaks for NTO NPs (at 0.75 V) and NTO MBs (at 0.90 V) correspond to the reduction of Ti^{4+}/Ni^{2+}.[34] The peaks at 0.10 V for NTO NPs and 0.20 V for NTO MBs are attributed to amorphous Li_2O formation.[25–27] At the initial anodic sweep, there are no obvious peaks. Subsequent sweeps, however, reveal distinct peaks for both NTO NPs and MBs. These peaks, observed at approximately 2.20 V for NTO NPs and 1.75 V for NTO MBs, correspond to the decomposition of Li_2O and the oxidation of Ni^0/Ti^{3+}.[25–27] The electrochemical reactions are presented as below[25,26]:

$$NiTiO_3 + 3Li^+ + 3e^- \rightarrow LiTiO_2 + Ni + Li_2O \quad (1)$$

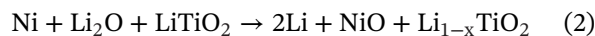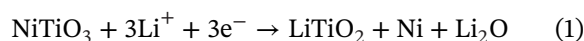$$Ni + Li_2O + LiTiO_2 \rightarrow 2Li + NiO + Li_{1-x}TiO_2 \quad (2)$$

Figure 6C displays cycling performance of both NTO electrodes during the initial 200 cycles at current density of 100 mA g^{-1}. For NTO MBs electrode, the first Coulomb efficiency is 62%. As the number of cycles increases, the Coulomb efficiency is stable at >99%. The observed capacity loss in the first cycle is related to the decomposition of the electrolyte and the formation of SEI film.[16,36,37] The SEI film consumes a part of charged lithium ions during the formation process, resulting in low Coulomb efficiency of the first cycle. With the stability of SEI film, the Coulomb efficiency increases gradually. Owing to significant volume change, the capacity of NTO NPs progressively declines, stabilizing at 212 mAh g^{-1}. Conversely, the capacity of NTO MBs decreases to 414 mAh g^{-1} after 30 cycles, before reaching a steady state at 410 mAh g^{-1}. In the first 30 cycles, the capacity reduction is primarily attributed to the formation of an organic polymer gel-like layer. After that, the capacity not only recovers but also remains stable. This stabilization can be attributed to three factors: (i) the organic polymer layer provides additional storage spaces for Li^+.[38–40] (ii) Activation of the NTO MBs electrode enhances the capacity.[41,42] (iii) The porous bar-like structure of NTO MBs increases the contact area between the NTO MBs anode and the electrolyte, mitigating significant volume changes and thereby maintaining structural stability during Li^+ insertion/extraction process.

Rate performance was assessed at various current densities, as depicted in Figure 6D. NTO MBs demonstrate average discharge capacities of 499, 348, 306, 272, and 233 mAh g^{-1} at 0.1, 0.2, 0.5, 1.0, and 2.0 A g^{-1}, respectively. Compared to NTO NPs, the average discharge of NTO MBs is higher at the same current density, indicating enhanced
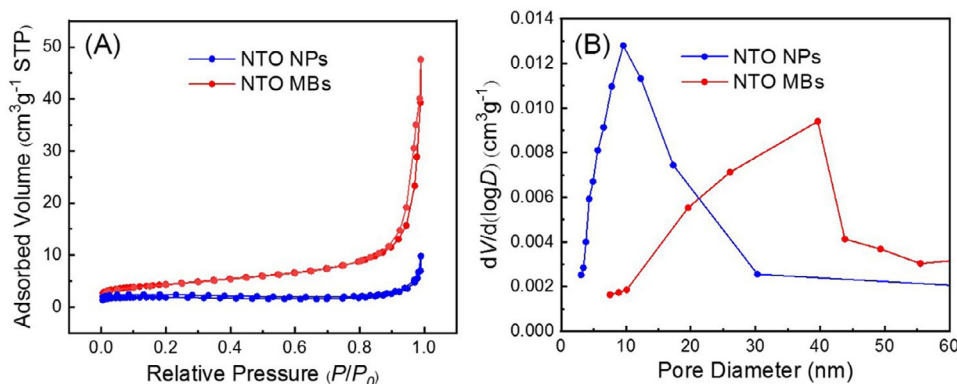
FIGURE 5 (A,B) Nitrogen adsorption–desorption isotherms and pore size distributions of NTO NPs and MBs. MB, microbar; NP, Nanoparticle.
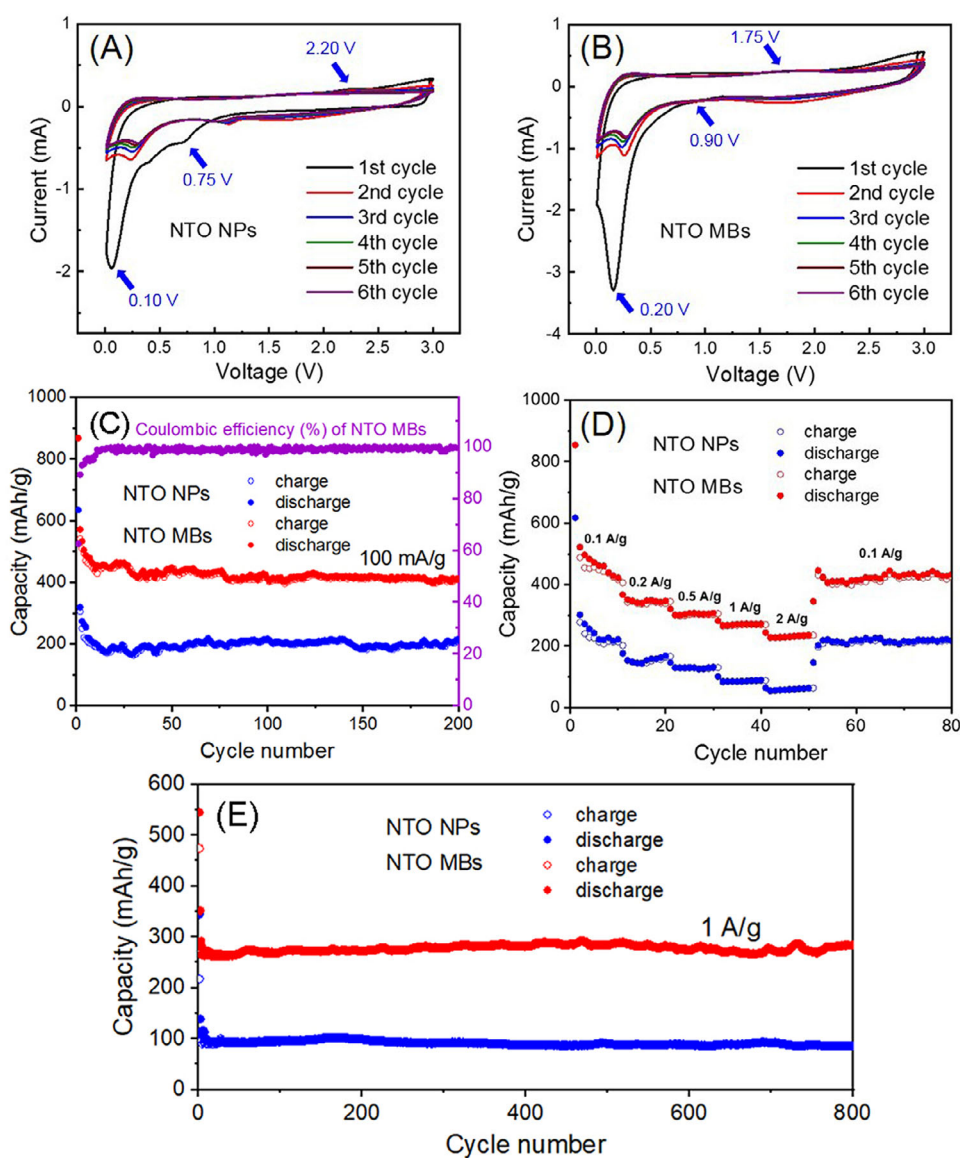

FIGURE 6 CV curves of NTO NPs (A) and MBs (B) electrodes at 0.3 mV s^{-1}. Cycling performance (C), rate capability (D) of NTO electrodes. (E) Long-term cycling performance of NTO electrodes at a high current density of 1 A/g. CV, Cyclic voltammetry; MB, microbar; NP, nanoparticle.
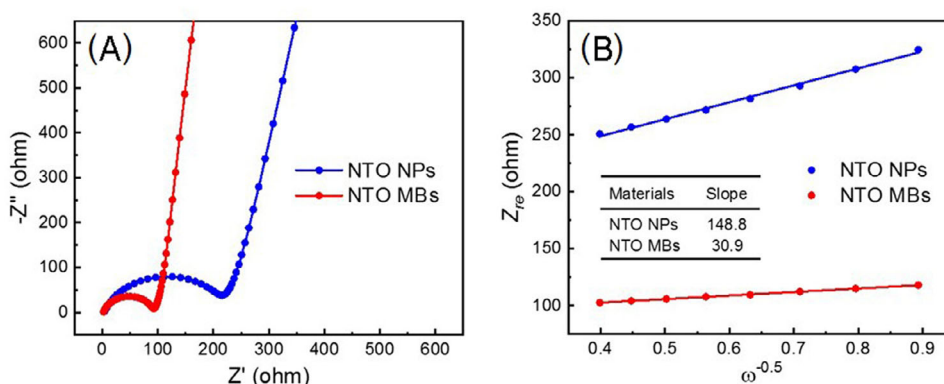
FIGURE 7 (A) EIS spectra of NTO NPs and MBs electrodes. (B) Graph of Z_{re} plotted against $\omega^{-0.5}$. EIS, Electrochemical impedance spectroscopy; MB, microbar; NP, nanoparticle.

rate performance. When the current density returns to 0.1 A g^{-1}, the capacity of NTO MBs peaks at 433 mAh g^{-1}, surpassing that of the NTO NPs electrode (217 mAh g^{-1}). To explore the long-term cycling performance under high current density, the NTO NPs and MBs electrodes were tested for 800 cycles at 1 A g^{-1} in Figure 6E. The discharge capacity of NTO MBs was maintained to 284 mAh g^{-1} after 800 cycles, far higher than that of NTO NPs (86 mAh g^{-1}). This enhancement can be attributed to the substantial specific surface area of NTO MBs, which offers additional sites for Li$^+$ ions during cycling, consequently boosting the lithium storage capacity.

To explore the electrochemical reaction kinetics, EIS tests were conducted before cycling. In Figure 7A, EIS spectrum is composed of a semicircle and an inclined line in high- and low-frequency regions, respectively. EIS spectrum of NTO MBs possesses smaller semicircle diameter than NTO NPs, which demonstrates that NTO MBs possess lower contact and charge transfer impedance. Moreover, the inclined line is connected with diffusion rate of Li$^+$. Furthermore, the slope of the inclined line, representing Li$^+$ diffusion, is steeper for NTO MBs than for NTO NPs, suggesting a faster Li$^+$ diffusion rate in NTO MBs. The Li$^+$ diffusion coefficient (D_{Li}) is calculated via the following equations[12,24,43,44]:

$$D_{Li} = \frac{R^2 T^2}{2A^2 n^4 F^4 C^2 \sigma^2} \quad (3)$$

where

$$C = \frac{n}{V} = \frac{m/M}{V} \quad (4)$$

and σ is deduced from Figure 7B by fitting the following expression:

$$Z_{re} = R_s + R_{ct} + \sigma \omega^{-0.5}. \quad (5)$$

F, R, and T are 96 485 C mol^{-1}, 8.314 J K^{-1} mol^{-1}, and 298.15 K, respectively. The electrode area A is 1.54 × 10^{-4} m^2. n is the number of the electrons single molecule involving the electronic transfer reaction. Li$^+$ concentration C is 1.10 × 10^4 mol m^{-3}. σ of NTO NPs and MBs is 148.8 and 30.9 Ω s$^{-0.5}$, respectively. D_{Li} of NTO MBs is 8.1 × 10^{-15} cm^2 s^{-1}, higher than that of NTO NPs (3.5 × 10^{-16} cm^2 s^{-1}), suggesting that NTO MBs possess stronger diffusion ability than NTO NPs. It can be concluded that the bar-like structure of NTO MBs is instrumental in promoting the rapid transport of electrons/Li$^+$.

To elucidate the lithium storage mechanism in detail, the XRD, SEM, and TEM measurements of NTO MBs electrode materials (after the first and 100th discharge cycle at a current rate of 100 mA g^{-1}) were carried out. Figure S1 shows XRD patterns of NTO MBs after first-cycle and 100th cycle. The XRD pattern of NTO after the initial cycle reveals diffraction peaks corresponding to both NTO and Ni, indicating partial reduction of Ni^{2+} to Ni^0. In contrast, the XRD pattern of the sample after 100th cycle displays a diffraction peak solely for Ni, suggesting complete reduction of Ni^{2+} to Ni^0. Figure S2A,B shows SEM images of first cycle and 100th cycle for NTO MBs, respectively. Both samples exhibit a bar-like morphology, indicating that NTO NBs possess excellent structural stability during cycling. Figure S3A,B displays typical BF images of first cycle and 100th cycle for NTO MBs, respectively. After many cycles, both samples still show a rod-like structure. Figure S3C,D shows the HRTEM images of first cycle and 100th cycle for NTO MBs, respectively. Figure S3D–F displays the enlarged HRTEM image in (C) and (D). The lattice spacings in Figure S3D,E are measured to be 3.68 and 2.08 Å, corresponding to the (0 1 2) plane of NTO and (1 1 1) plane of Ni, respectively. The lattice spacings in Figure S3F are determined to be 1.80 and 1.80 Å, which correspond to the (2 0 0) and (0 2 0) planes of Ni, respectively. After the first
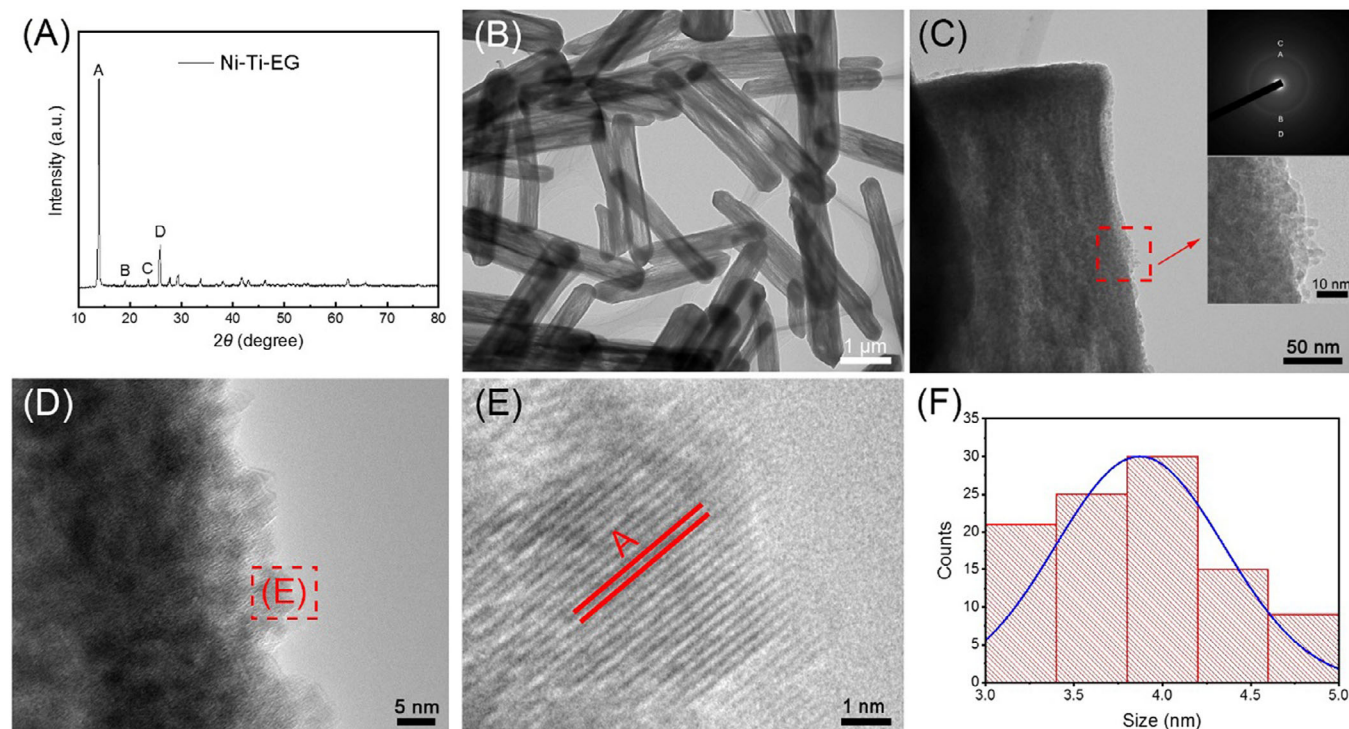
FIGURE 8 (A) XRD pattern of Ni–Ti–EG. (B) Typical BF TEM image and of Ni–Ti–EG microbars. (C) TEM image of Ni–Ti–EG microbar. Inset shows the SAED pattern and enlarged TEM image of the regions surrounded by a rectangle. (D) HRTEM image of Ni–Ti–EG microbar. (E) Enlarged HRTEM image in (D). (F) Size distribution of small NPs in Ni–Ti–EG microbar. BF, bright field; HRTEM, high-resolution transmission electron microscope; NP, nanoparticle; SAED, selected area electron diffraction; TEM, transmission electron microscope; XRD, X-ray diffraction;.

cycle for NTO MBs electrode, Ni^{2+} in NTO was partially reduced to Ni, corresponding to the peak of 0.90 V. After 100 discharge cycles, Ni^{2+} was fully reduced to Ni, which can correspond to the peak of 1.75 V in the multiple cycles. These are in accordance with XRD results in Figure S1.

The electrochemical properties for NTO electrodes are closely related to their morphological features. NTO NPs electrode suffered from powderization of particles and large volume changes during cycling. In contrast, NTO MBs are formed of numerous NPs, and the average size of these particles is smaller than that of NTO NPs. Therefore, the NTO MBs possess larger specific surface area, facilitating an increased number of lithium storage sites. This property augments specific capacity and aids in mitigating volume expansion during the charge and discharge processes.

To understand the impact of morphology, particularly the bar-like structure, on the enhancement of material electrochemical performance, we explored the growth mechanism of NTO MBs by characterizing their precursor. The XRD pattern of the precursor exhibits a strong low-angle reflection, as shown in Figure 8A, which is usually ascribed to the lamellar structure of metal–ethylene glycol (metal–EG) complexes.[45–47] Moreover, the lack of structural information about this material makes it impossible to identify the precursor by XRD. Therefore, the precursor of NTO MBs can be referred to as Ni–Ti–EG. Meanwhile, the sharp peaks observed in the XRD pattern indicate the high crystallinity of Ni–Ti–EG. The BF TEM image in Figure 8B reveals a uniform bar-shaped morphology with even dimensions for Ni–Ti–EG. This indicates that EG plays a significant role in the formation of the bar-like morphology of the product. Upon closer examination of the enlarged TEM image in Figure 8C, it is evident that the Ni–Ti–EG MB is composed of many small NPs. The inset SAED pattern also confirms the polycrystalline structure of Ni–Ti–EG MB. The four diffraction rings in the SAED pattern, from inner to outer, correspond to the crystal planes A, B, C, and D as identified in the XRD pattern. Furthermore, the magnified TEM image depicted in Figure 8D provides clear evidence of the presence of numerous NPs within the precursor. The lattice spacing in Figure 8E is determined to be 3.43 Å, corresponding to the A-plane in the XRD pattern of Ni–Ti–EG MB. In Figure 8F, the NPs found in NTO MBs exhibit a size distribution ranging from 3 to 5 nm, with an average diameter of 3.9 nm.

Based on the results presented above, a plausible growth mechanism for NTO MBs is proposed, as shown in Figure 9. To synthesize these MBs, NA and TBT were used as the sources of Ni and Ti, respectively, while
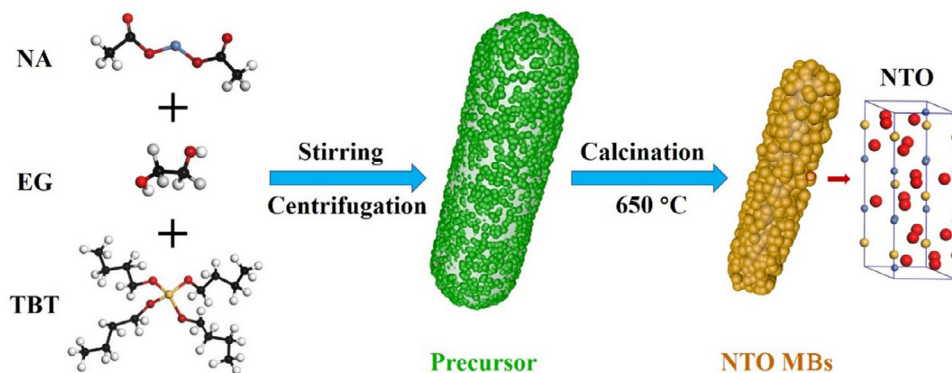
FIGURE 9 Schematic illustration of NTO MBs formation. MB, microbar.

EG was employed as a ligand to modulate the morphology of the product. It is widely recognized that EG is a bidentate ligand that can react with metal ions to form a metal–glycolate polymer due to its coordination ability with transition metal ions.[48] In our experiment, Ni and Ti ions orderly coordinate with EG to form a Ni–Ti–EG complex, which are subsequently condensed and assembled into bar-like precursors under the influence of van der Waals interactions. Subsequently, the organic species present within the bar-like precursor gradually undergo decomposition during the calcination process in air. Meantime, the small-sized Ni–Ti–EG NPs embedded internally within the precursor MBs transform into crystalline NTO NPs, and then adjacent small NTO NPs grow into large ones through orientation adjustment and coalescence process. In this process, despite the reduction in the micrometer-scale dimensions of the precursor MBs, their overall morphology is maintained. Consequently, the final product consists of NTO MBs with a porous structure. The improved electrochemical performances of NTO MBs can be attributed to their unique porous bar-like structure, composed of numerous NPs, which can provide a substantial storage space for Li$^+$ ions owing to larger specific surface area of MBs.

4 | CONCLUSIONS

In summary, the self-assembly of NTO NPs into MBs is accomplished through manipulation of the solvent employed in the solvothermal synthesis process. NTO MBs demonstrate superior capacity retention and cycling stability compared to NTO NPs when employed as anode materials in LIBs. This enhanced performance can be attributed to the unique porous bar-like structure of NTO MBs, which offers a larger specific surface area, thereby enabling significant Li$^+$ ion storage capacity. Furthermore, the porous structure facilitates rapid diffusion of Li$^+$ ions

and electron transfer. Based on a comprehensive investigation of the precursor, a plausible growth mechanism is proposed for the formation of NTO MBs to gain a thorough understanding of the fundamental mechanisms governing the achieved performance enhancement through morphology adjustment. The findings in this study provide valuable insights into controlling the morphology of NTO MBs, thereby enabling the rational design and synthesis of tailored materials with enhanced performance for LIBs.

REFERENCES

1. Yan JQ, Huang H, Tong JF, Li W, Liu XH, Zhang HX, et al. Recent progress on the modification of high nickel content NCM: coating, doping, and single crystallization. Interdiscip Mater. 2022;1(3):330–53.
2. Zhang BW, Ren L, Wang YX, Xu X, Du Y, Dou SX. Gallium-based liquid metals for lithium-ion batteries. Interdiscip Mater. 2022;1(3):354–72.
3. Zheng JM, Engelhard MH, Mei DH, Jiao SH, Polzin BJ, Zhang JG, et al. Electrolyte additive enabled fast charging and stable cycling lithium metal batteries. Nat Energy. 2017;2(3):17012.
4. Hao SJ, Sheng XL, Xie F, Sun M, Diao FY, Wang YQ. Electrospun carbon nanofibers embedded with heterostructured NiFe$_2$O$_4$/Fe$_{0.64}$Ni$_{0.36}$ nanoparticles as an anode for

high-performance lithium-ion battery. J Energy Storage. 2024;80:110412.

5. Goodenough JB, Park KP. The Li-ion rechargeable battery: a perspective. J Am Chem Soc. 2013;135:1167–76.

6. Xie F, Sun M, Sheng XL, Zhang QY, Ling ZB, Hao SJ, et al. Graphene-wrapped Fe_2TiO_5 nanoparticles with enhanced performance as lithium-ion battery anode. Mater Lett. 2024;358:135877.

7. Hummers WS, Offeman RE. Preparation of graphitic oxide. J Am Chem Soc. 1958;80:1339.

8. Amine K, Kanno R, Tzeng YH. Rechargeable lithium batteries and beyond: progress, challenges, and future directions. MRS Bull. 2014;39(5):395–405.

9. Li T, Gao SW, Li K, Liu GJ, Sheng XL, Shang DW, et al. Tailoring the phase evolution of molybdenum-based nanocrystals in carbon nanofibers for enhanced performance of lithium-ion batteries. J Alloy Compd. 2023;934:168042.

10. Li YH, Sun H, Cheng XP, Zhang YF, Zhao KJ. In-situ TEM experiments and first-principles studies on the electrochemical and mechanical behaviors of alpha-MoO_3 in Li-ion batteries. Nano Energy. 2016;27:95–102.

11. Liu J, Li T, Zhang H, Zhao WW, Qu LJ, Chen SJ, et al. Electrospun strong, bioactive, and bioabsorbable silk fibroin/poly (L-lactic-acid) nanoyarns for constructing advanced nanotextile tissue scaffolds. Mater Today Bio. 2022;14:100243.

12. Sheng XL, Li T, Sun M, Liu GJ, Zhang QY, Ling ZB, et al. Flexible electrospun iron compounds/carbon fibers: phase transformation and electrochemical properties. Electrochim Acta. 2022;407:139892.

13. Diao FY, Wang YQ. Transition metal oxide nanostructures: premeditated fabrication and applications in electronic and photonic devices. J Mater Sci. 2018;53(6):4334–59.

14. Wu SH, Qi Y, Shi W, Kuss M, Chen SJ, Duan B. Electrospun conductive nanofiber yarns for accelerating mesenchymal stem cells differentiation and maturation into Schwann cell-like cells under a combination of electrical stimulation and chemical induction. Acta Biomater. 2022;139:91–104.

15. Ouyang BX, Chen T, Qin R, Liu PG, Fan XW, Wang J, et al. Bimetal-organic-framework derived $CoTiO_3$/C hexagonal micro-prisms as high-performance anode materials for metal ion batteries. Mater Chem Front. 2021;5(15):5760–68.

16. Wang X, Cheng WJ, Hu JQ, Su Y, Kong XG, Uemura S, et al. Mesocrystalline effect in a $NiTiO_3$/TiO_2 nanocomposite for enhanced capacity of lithium-ion battery anodes. Inorg Chem Front. 2022;9(9):2055–67.

17. Liu H, Li ZP, Sun HY, Lu QF. Electrospun Fe_2TiO_5–TiO_2@graphene nanofibers as highly durable insertion anode with enhanced lithium storage properties. Energy Technol. 2020;8(7):2000215.

18. Guo SM, Wang Y, Chen LJ, Pan D, Guo ZH, Xia SB. Porous TiO_2–$FeTiO_3$@carbon nanocomposites as anode for high-performance lithium-ion batteries. J Alloy Compd. 2021;858:157635.

19. Gao RM, Jiao Z, Wang Y, Xu LQ, Xia SS, Zhang HJ. Eco-friendly synthesis of rutile TiO_2 nanostructures with controlled morphology for efficient lithium-ion batteries. Chem Eng J. 2016;304:156–64.

20. Ge MZ, Cao CY, Huang JY, Li SH, Chen Z, Zhang KQ, et al. A review of one-dimensional TiO_2 nanostructured materials for environmental and energy applications. J Mater Chem A. 2016;4(18):6772–801.

21. Zhang YQ, Du F, Yan X, Jin YM, Zhu K, Wang X, et al. Improvements in the electrochemical kinetic properties and rate capability of anatase titanium dioxide nanoparticles by nitrogen doping. ACS Appl Mater Int. 2014;6(6):4458–65.

22. Yang ZG, Choi D, Kerisit S, Rosso KM, Wang DH, Zhang J, et al. Nanostructures and lithium electrochemical reactivity of lithium titanites and titanium oxides: a review. J Power Sources. 2009;192(2):588–98.

23. Guo SM, Liu JR, Qiu S, Wang YR, Yan XR, Wu NN, et al. Enhancing electrochemical performances of TiO_2 porous microspheres through hybridizing with $FeTiO_3$ and nanocarbon. Electrochim Acta. 2016;190:556–65.

24. Sun M, Sheng XL, Li SJ, Cui ZP, Li T, Zhang QY, et al. Construction of porous $CoTiO_3$ microrods with enhanced performance as lithium-ion battery anode. J Alloy Compd. 2022;10(11):166809.

25. Wang YA, Chen XY, Wang QY, Zeng YQ, Liao K, Zhang SL, et al. Novel 3D hierarchical bifunctional $NiTiO_3$ nanoflower for superior visible light photoreduction performance of CO_2 to CH_4 and high lithium storage performance. Energy. 2019;169:580–86.

26. Majumder T, Das D, Majumder SB. Investigations on the electrochemical characteristics of electrophoretically deposited $NiTiO_3$ negative electrode for lithium-ion rechargeable cells. J Phys Chem Solids. 2021;158:110239.

27. Li M, Fan XL, Xiao XZ, Huang X, Jiang YQ, Chen LX. Ternary perovskite nickel titanate/reduced graphene oxide nano-composite with improved lithium storage properties. RSC Adv. 2016;6(66):61312–18.

28. Huang ZD, Zhang TT, Lu H, Masese T, Yamamoto K, Liu RQ, et al. Grain-boundary-rich mesoporous $NiTiO_3$ micro-prism as high tap-density, super rate and long life anode for sodium and lithium ion batteries. Energy Storage Mater. 2018;13:329–39.

29. Zou JJ, Liu B, Liu HQ, Ding YH, Xin T, Wang YQ. Facile synthesis of interconnected mesoporous $ZnMn_2O_4$ nano-peanuts for Li-storage via distinct structure design. Mater Res Bull. 2018;107:468–76.

30. Tang YW, Wu LJ, Xiao L, Wen DQ, Guo QW, Liang WC. Porous $CoTiO_3$ microbars as super rate and long life anodes for sodium ion batteries. Ceram Int. 2018;44(15):18025–31.

31. Pavithra C, Madhuri W. Electrical and magnetic properties of $NiTiO_3$ nanoparticles synthesized by the sol-gel synthesis method and microwave sintering. Mater Chem Phys. 2018;211:144–49.

32. Jing PP, Lan W, Su Q, Yu ML, Xie EQ. Visible-light photocatalytic activity of novel $NiTiO_3$ nanowires with rosary-like shape. Sci Adv Mater. 2014;6(3):434–40.

33. Jiang K, Pham TT, Kang SG, Men Y, Shin EW. Modification of the structural properties of $NiTiO_3$ materials by transition metal dopants: the dopant size effect. J Alloy Compd. 2018;739:393–400.

34. Li Q, Wang HJ, Ma JJ, Yang X, Yuan R, Chai YQ. Porous Fe_2O_3–C microcubes as anodes for lithium-ion batteries by rational introduction of Ag nanoparticles. J Alloy Compd. 2018;735:840–46.

35. Inamdar AI, Kalubarme RS, Kim J, Jo Y, Woo H, Cho S, et al. Nickel titanate lithium-ion battery anodes with high reversible capacity and high-rate long-cycle life performance. J Mater Chem A. 2016;4(13):4691–99.

36. Xu JJ, Ding W, Zhao WL, Zhao W, Hong ZL, Huang FQ. In situ growth enabling ideal graphene encapsulation upon mesocrystalline MTiO$_3$ (M = Ni, Co, Fe) nanorods for stable lithium storage. ACS Energy Lett. 2017;2(3):659–63.

37. Majumder T, Das D, Majumder SB. Nickel Titanate–GO composite as negative electrode for lithium and sodium ion batteries. Mater Lett. 2021;301:130293.

38. Sun M, Li SJ, Zou JJ, Cui ZP, Zhang QY, Schiettekatte F, et al. Graphene-wrapped ZnMn$_2$O$_4$ nanoparticles with enhanced performance as lithium-ion battery anode materials. Nano. 2020;15(9):2050117.

39. Cui ZP, Sun M, Liu HQ, Li SJ, Zhang QY, Yang CP, et al. Double-shell SnO$_2$@Fe$_2$O$_3$ hollow spheres as a high-performance anode material for lithium-ion batteries. Crystengcomm. 2020;22(7):1197–208.

40. Sun M, Cui ZP, Liu HQ, Li SJ, Zhang QY, Sheng XL, et al. Graphene-wrapped FeOOH nanorods with enhanced performance as lithium-ion battery anode. Nano. 2021;16(1):2150005.

41. Liu HQ, Zou JJ, Ding YH, Liu B, Wang YQ. Novel FeOOH corner-truncated tetragonal prisms: crystal structure, growth mechanism and lithium storage properties. J Appl Electrochem. 2019;49(7):657–69.

42. Xie F, Sheng XL, Ling ZB, Hao SJ, Zhang QY, Sun M, et al. Flexible electrospun iron/manganese-based compounds/carbon fibers: phase transformation and electrochemical properties. Electrochim Acta. 2023;470:143288.

43. Li JK, Wang D, Zhou JS, Hou L, Gao FM. MOF-derived in situ synthesized carbon-coated ilmenite cobalt titanate nanocrystalline, high-stability lithium-ion batteries. J Alloy Compd. 2019;793:247–58.

44. Wang J, Polleux J, Lim J, Dunn B. Pseudocapacitive contributions to electrochemical energy storage in TiO$_2$ (anatase) nanoparticles. J Mater Chem C. 2007;111(40):14925–31.

45. Tian CG, Li W, Zhang Q, Pan K, Fu HG. Controllable fabrication of various ZnO micro/nanostructures from a wire-like Zn–EG–AC precursor via a facile solution-based route. Mater Res Bull. 2011;46(8):1283–89.

46. Larcher D, Sudant G, Patrice R, Tarascon JM. Some insights on the use of polyols-based metal alkoxides powders as precursors for tailored metal-oxides particles. Chem Mater. 2003;15(18):3543–51.

47. Wang YL, Jiang XC, Xia YN. A solution-phase, precursor route to polycrystalline SnO$_2$ nanowires that can be used for gas sensing under ambient conditions. J Am Chem Soc. 2003;125(52):16176–77.

48. Qu Y, Zhou W, Ren ZY, Du SC, Meng XY, Tian GH, et al. Facile preparation of porous NiTiO$_3$ nanorods with enhanced visible-light-driven photocatalytic performance. J Mater Chem. 2012;22(32):16471–76.

SUPPORTING INFORMATION

Additional supporting information can be found online in the Supporting Information section at the end of this article.